IEEE Access
Multidisciplinary | Rapid Review | Open Access Journal

Digital Object Identifier

A Guided-Ensembling Approach for Cell Counting in Fluorescence Microscopy Images

C. EMRE DEDEAGAC[1], (Graduate Student Member, IEEE), CAN F. KOYUNCU[2,3], MICHELLE M. ADAMS[4,5], CAGATAY EDEMEN[6], (Senior Member, IEEE), BERK C. UGURDAG[7], (Student Member, IEEE), N. ILGIM ARDIC-AVCI[4], H. FATIH UGURDAG[6], (Senior Member, IEEE)

[1]Department of Computer Science, Ozyegin University, Istanbul, Turkiye.
[2]Department of Biomedical Engineering, Georgia Institute of Technology, Atlanta, GA, USA.
[3]Emory University, Atlanta, GA, USA.
[4]Interdisciplinary Graduate Program in Neuroscience, National Nanotechnology Research Center (UNAM), Ankara, Turkiye.
[5]Department of Psychology, Bilkent University, Ankara, Turkiye.
[6]Department of Electrical and Electronics Engineering, Ozyegin University, Istanbul, Turkiye.
[7]Department of Computer Science, Georgetown University, Washington, DC, USA.

Corresponding author: Can F. Koyuncu (email: canfkoyuncu@gmail.com).

ABSTRACT Although deep learning and computer vision based approaches have demonstrated success in the field of cell counting and detection in microscopic images, they continue to have certain limitations. More specifically, they experience an overall increase in false positives when dealing with cell populations that show high density and heterogeneity. Existing approaches require the reselection of parameters for each new dataset to improve the accuracy of cell counting. Therefore, it is necessary to revise the fundamental models for each new microscopic image. This study introduces a novel neural network-based method that eliminates the need for retraining by combining the pretrained Cellpose and Stardist models. The accuracy of our proposed approach was evaluated on a variety of microscopic images. Despite variations in cell densities, our proposed approach demonstrated a notably improved cell counting performance in comparison to solely utilizing the Cellpose and Stardist models.

INDEX TERMS cell counting, cell detection, deep learning, ensemble learning

I. INTRODUCTION

THE traditional way of cell analysis in clinical practice involves microscopic observation of a tissue sample. The process allows us to classify different cellular characteristics and evaluate the cellular structure precisely. The initial step of such analysis usually requires cell segmentation [1]–[11], cell detection [12], [13], or cell counting [14]. Although experts can extract limited information through counting cells, it is still an acceptable approach in clinical practice due to its practicality [15]. As one might expect, manual counting of cells is a very time-consuming and labor-intensive task with several potential drawbacks, including (i) risk of human error, (ii) lack of objectivity, (iii) poor reproducibility, and (iv) low throughput. In terms of human error, the issues include misidentification and missed cells due to fatigue or distraction. Moreover, it is subjective and dependent on the expertise of the observer, resulting in differences between the observers [16]. Reproducibility is another problem that leads to variability between observers and differences across different laboratories or studies. It is one of the critical concerns in research, and several studies have highlighted the variability in manual cell counting results [17]. Moreover, manual cell counting may be impractical for large-scale studies or experiments requiring high throughput. Due to these significant limitations, semi- or fully autonomous techniques based on image processing and neural networks for automated cell counting have been developed. The development of computerized cell counting software will significantly impact biological research and clinical practice, facilitating faster, more objective, and more standardized cell counting than manual methods [18].

II. RELATED WORK

Conventional image processing-based techniques are straightforward methodologies that do not require labeled data and can resolve a specific problem with fewer lines of code compared to neural network-based methods [8], [9]. Nevertheless, they are susceptible to hyperparameter settings and necessitate manual adjustments when applied to diverse datasets. Furthermore, when confronted with cell populations exhibiting high density and heterogeneity, these methods generally tend to have a decline in precision or an increase in false

positives [8], [19], [20]. Unlike traditional methods, state-of-the-art cell detection techniques rely on training deep neural networks [4]–[6], [13]. Achieving a high level of accuracy in cell counting using neural network-based models demands extensive and data-intensive training. Despite the need for a substantial amount of data and comprehensive annotation, Cellpose [4], [5] and Stardist [6] have demonstrated particularly promising outcomes and have garnered considerable attention recently. Their popularity is primarily due to their remarkable accuracy on specific datasets. Nevertheless, they are resistant to interpretability, and the performance highly depends on the quality and appropriateness of the training dataset.

Despite being popular, Cellpose and Stardist are still susceptible to variations in cell density, shape, and size. For instance, Kleinberg et al. [21] revealed that the Stardist trained model showed greater precision in estimating cell counts particularly in regions where cells were in close proximity or even over-clumped, in comparison to Cellpose. However, in situations where the cell distribution was sparse, Stardist had a higher likelihood of producing inaccurately detected cells, whereas Cellpose appeared to exhibit greater resilience under such conditions. These findings suggest that utilizing an ensembling technique can harness the strengths of individual methods, leading to a substantial improvement in cell detection performance.

Ensemble approaches are a sophisticated method for constructing multiple models with the goal of achieving improved results [22]. There exists only a limited number of studies on the subject of cell counting through an ensembling approach [23]–[28]. For instance, [27] ensembles the output of three models, where each model utilized the same architecture but trained on different image batches. As another example, [28] uses an ensembling methodology to combine the outputs of five models to segment cells from 3D volume. Each model was trained with a different number of frames, i.e., a model seeing one frame, a model seeing three frames, etc. This way of ensembling helps eliminate low-confidence markers and merge overlapping segmentations to detect and count mimicked circulating tumor cells (mCTC). On the other hand, all of these studies necessitate training or fine-tuning of every model to enhance predictive accuracy, which is time-consuming and laborious. Due to the challenges associated with training, there exists a significant demand for a novel approach, particularly in the context of ensemble approaches.

There are two main highlights of this study:

- We introduce a novel guided-ensembling technique that leverages two state-of-the-art cell detection methods, which have been trained with billions of cell images, with no additional retraining or fine-tuning. Experiments on three different cell counting datasets have shown that the guided-ensembling approach outperformed the separately used techniques.
- Contrary to most of the existing studies in this domain, we compare the results in images with high congestion diversity and tissue noise, which creates many artifacts in sparse regions and causes vague segregation of cells in congested regions. We show the effects of the heuristic approach on these harder-to-process images.

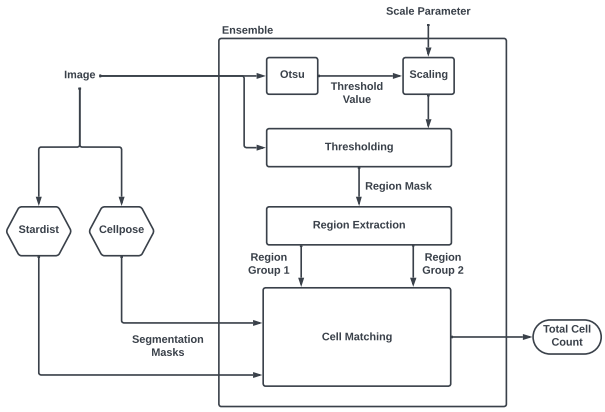

FIGURE 1. Top level view of the process.

III. METHODOLOGY

This approach involves the integration of state-of-the-art cell segmentation models with a hard decision-making mechanism that relies on the size of the cell clusters. Fig. 1 shows the block diagram of the proposed approach. The objective of the proposed approach is to take advantage of the need for additional training by finding optimal regions for each model. Due to variations in training sets and network structures across models, each model is expected to show outstanding detection performance for specific areas in a given image. To maximize the performance of different models, the proposed study attempts to solve the cell counting problem by implementing a two-step approach. In the first phase, the algorithm produces segmentation masks of an image. The next step includes the utilization of Otsu's algorithm to extract areas containing cellular presence and then assigning each area to a model based on cellular density.

For convenience, in the rest of the paper M_{CP}, M_{SD}, and M_E will denote three different detection methods, Cellpose, Stardist, and the proposed guided ensembling methods, respectively. The proposed approach will be explained comprehensively in the following sections.

A. CELL SEGMENTATION VIA CELLPOSE AND STARDIST

For M_{CP}, we used the pretrained "cyto" model, which predicts the probability of a pixel being inside a cell and the flows of pixels toward the center of a cell in X and Y for each pixel. It utilizes a standard U-Net backbone with 32 layers of blocks. Each block consists of $3x3$ convolution and max pooling (or upsampling). M_{CP} was trained with 540 images that have more than 70,000 cells.

As for M_{SD}, we used the pre-trained model "2D_versatile_fluo", which was trained with a subset of the DSB2018 nuclei

segmentation dataset [29]. It predicts for every pixel a *star-convex polygon* for the cell instance at that position. On top of the popular U-Net architecture [30], an additional 33 convolutional layer with 128 channels (and relu activations) is added to avoid *fight over features*. Both methods accept a grayscale image (R-channel for D_{ORIG}), I, as input.

B. GUIDED-ENSEMBLING APPROACH

The ensemble stage uses the original image I with the segmentation masks S_{CP} and S_{SD}. Users can fine-tune the algorithms' decision-making mechanisms by adjusting two external parameters, namely P_{scale} and $P_{threshold}$. The variable P_{scale} is a numerical value within the interval [0,1], which represents the scaling factor applied to the threshold value obtained through Otsu's algorithm, as utilized in Section III-B1. The variable $P_{threshold}$ is a parameter that can assume any positive integer value and serves to denote the threshold level for the pixel area covered by a connected component. Sections III-B2 and IV-C provide an additional explanation of the utilization of the parameters.

Guided-Ensembling Algorithm

Input: image I, area threshold $P_{threshold}$, postscale for otsu P_{scale}
Output: number of cells NoC
Initial: $NoC \leftarrow 0$
$S_{CP} \leftarrow$ GENERATE_CELLPOSE_MASK(I)
$S_{SD} \leftarrow$ GENERATE_STARDIST_MASK(I)
$TH \leftarrow$ FIND_OTSU_THRESHOLD_VALUE(I)
/* TH: the value found by Otsu's algorithm */
$B \leftarrow$ BINARIZE_IMAGE$(I, TH * P_{scale})$
/* B: binary mask obtained by global thresholding */
$REGIONS \leftarrow$ EXTRACT_REGION_AND_LABEL(B)
/* REGIONS: A list of connected components in B */
for each region in REGION **do**
  if region.area < $P_{threshold}$ **then**
    /* Add the number of markers overlapping with region */
    $NoC \mathrel{+}=$ COUNT_MARKERS$(region, S_{SD})$
  else
    $NoC \mathrel{+}=$ COUNT_MARKERS$(region, S_{CP})$
  end if
end for

Initially, the algorithm produces a grayscale version of the original image and then employs thresholding methodologies to isolate areas that are densely occupied by cells. The congested cell groups can be identified by the threshold algorithm and indicated by each connected component produced by the threshold algorithm. The presence of a significant cluster is indicated by a large number of cells showing minimal contrast variation with the surrounding background and being near neighboring cells within the corresponding area. The algorithm's cell matching phase involves iterating through each region and determining the cells to be included from the input segmentation masks. The total number of cells in all areas is then computed by adding up the counted cells.

Although the proposed methodology employs sophisticated deep learning algorithms, its overall time complexity is linear with respect to the number of parameters in the deep learning architectures. The algorithm described consists of three primary phases: pre-processing, ensembling, and post-processing. In both the pre-processing and post-processing phases, each method utilized demonstrates linear complexity relative to the number of pixels in an image, denoted as O(n), where n signifies the pixel count. As these methods are executed sequentially, the overall complexity remains O(n). The ensemble phase involves generating predictions using two algorithms and subsequently integrating their outputs. Each prediction requires a single forward pass through the Stardist and Cellpose networks, characterized by a complexity of O(m), where m represents the number of learner parameters within the networks. The integration of results is constrained by the pixel count, resulting in the complexity of the ensemble phase being O(max(n, m)). Therefore, the comprehensive complexity of the algorithm is O(max(n, m)).

1) Binary Mask Generation and Region Extraction

At first, the ensembling procedure will determine a threshold value by means of Otsu's algorithm. Then, this value will be adjusted proportionally using an external parameter denoted as P_{scale}. The threshold value needs to be adjusted to include cells that have lower brightness values. This procedure results in the creation of certain insignificant artifacts that are related to tissue noise. The algorithm prevents artifacts by eliminating regions that do not meet the minimum size threshold to be categorized as cells. Following the generation of the mask, the region props tool in MATLAB is used to extract each region.

2) Matching and Counting Cells

The algorithm evaluates each region and determines the appropriate segmentation mask to include the cells. The algorithm analyzes the area size of each cell and then examines the overlapping cells from S_{SD} if the area size exceeds the specified threshold parameter. If the value falls below the specified threshold parameter $P_{threshold}$, the algorithm proceeds to search for overlapping cells in S_{CP}. For a cell to be considered part of a given region, it is necessary that it has a minimum overlap of 50%. This method additionally assigns new labels to all cells obtained from the segmentation masks and transfers them to an intermediary segmentation mask. The algorithm provides the total number of cells of the intermediate mask.

IV. EXPERIMENTS

This section presents the experimental findings for each dataset.

A. DATASETS

Three datasets were used in the experimentation. The Broad Bioimage Benchmark Collection website offers two publicly accessible datasets, namely, BBBC004 [31], [32], and BBBC039, as documented in [33]. Each of the mentioned

datasets consists of images obtained through fluorescence microscopy. From now on, the datasets shall be denoted as D_{ORIG}[1], D_{C4}, and D_{C39}, respectively. Table 1 presents an overview of the datasets mentioned.

Dataset Name	Number of Images	Image Resolution
D_{ORIG}	290	1924x2572
D_{C39}	200	520x696
D_{C4}	100	950x950

TABLE 1. Dataset names, number of images, and image resolutions.

The sample denoted as D_{ORIG} includes fish brain cells that have been magnified by a factor of 20. Cells show significant variability in terms of counts, congestion, and tissue noise. The images provided have high resolution, measuring 2572 pixels in width and 1924 pixels in height. On average, the diameter of the cells measures 20 pixels. All cellular structures have uniform sizes and shapes. A total of 290 images have been reported, each with a reported count of the total number of cells in existence. A total of twelve images in the dataset have point annotations.

The datasets denoted as D_{C4} and D_{C39} include fluorescent microscopy images that are supported by annotations of the cell count and foreground. These properties provide consistency to the outcomes in relation to D_{ORIG}, thus enhancing the reliability of the following comparisons. The images show different cell congestion patterns that match the characteristics of the D_{ORIG} dataset. The images obtained from D_{C4} and D_{C39} show comparatively lower levels of congestion and tissue noise, making them easier to process using state-of-the-art cell counting models in contrast to D_{ORIG}.

The dataset denoted by D_{C4} comprises artificially produced cellular images showing different levels of congestion probabilities, namely 0%, 15%, 30%, 45%, and 60%. One hundred images have been distributed into five subsets, each showing distinct levels of congestion. Each image contains a total of 300 individual units. Foreground segmentation can also be obtained. The dimensions of each image are 950 pixels for both width and height.

The dataset denoted by D_{C39} includes a total of 200 U2OS cellular images. The resolution of each image is 520x696 pixels. The ground truth data related to foreground segmentations, outlines, and cell counts are accessible.

B. RESULTS

This subsection provides an analysis of the results obtained from the proposed approach. Trendlines are included in the cell count plots for each method to enable a comprehensive comparison. The results of the cell counts obtained by each method for each manual cell count can be seen in Fig. 2. Note that some images show identical manual cell counts, which allows for the possibility of a method that includes multiple markers that are vertically aligned. Each method has a trendline that fits its results. The trendline for the variable M_E shows a higher degree of closeness to the results of manual counting, in contrast to the trendlines of M_{CP} and M_{SD}. This implies that the accuracy of M_E is better in general. The values of P_{scale} and $P_{threshold}$ for the given dataset have been set as 0.8 and $10,000$, respectively.

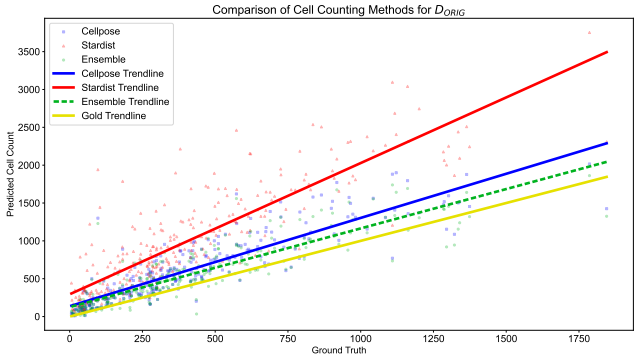

FIGURE 2. Cell count results for D_{ORIG}. The X-axis denotes manual cell counts, and Y-axis denotes calculated cell counts for images. Red triangles indicate Stardist results. Blue squares indicate Cellpose results. Green circles indicate ensemble results. The gold trendline indicates the manual counts.

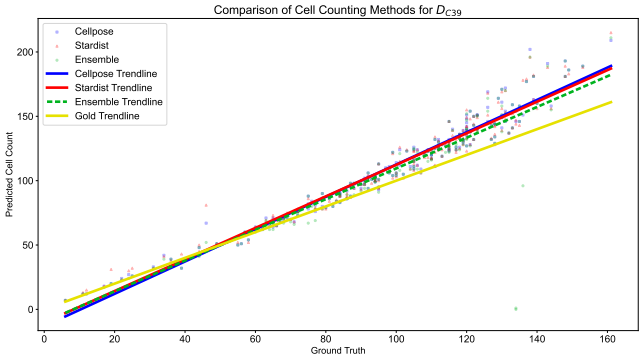

FIGURE 3. Cell count results for D_{C39}. The X-axis denotes manual cell counts, and Y-axis denotes calculated cell counts for images. Red triangles indicate Stardist results. Blue squares indicate Cellpose results. Green circles indicate ensemble results. The gold trendline indicates the manual counts.

The results of the calculated cell count for each manual cell count are presented in Fig. 3. The graphical representation shows characteristics identical to those of Fig. 2. The closeness between the green trendline (M_E) and the gold trendline (manual counts) is visible. The present dataset has values of 0.8 and $10,000$ for P_{scale} and $P_{threshold}$, respectively.

The performance of all methods for the D_{C4} dataset is shown in Fig. 4. Given that the initial subset showed a congestion probability of exactly 0%, all methods effectively achieved cell segmentation. As the congestion rate increased, all techniques showed a deviation from the ground truth values. It is notable that the trendlines for M_E and M_{CP} show a significant degree of overlap. Although the proposed

[1]Bilkent University Local Animal Ethics Committee (HADYEK) approved the animal ethics protocols of this data with the following approval dates and numbers: July 10, 2015, with protocol number 2015/31 and February 21, 2018, with protocol number 2018/4.

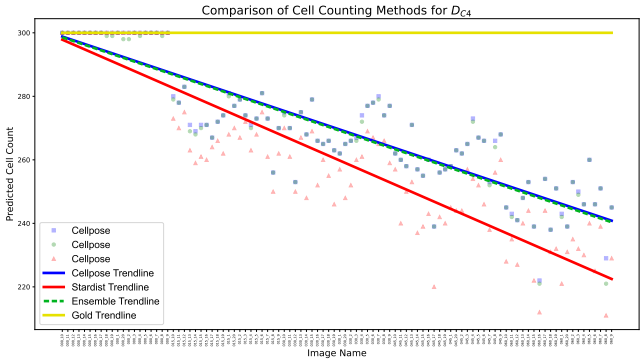

FIGURE 4. **Cell count results for D_{C4}. The X-axis denotes each image in the dataset, and Y-axis denotes calculated cell counts for images. Red triangles indicate Stardist results. Blue squares indicate Cellpose results. Green circles indicate ensemble results. The gold trendline indicates the manual counts.**

approach did not result in a statistically significant improvement in this particular dataset, the results indicate that the overall performance is limited by the benchmark methods. The values of P_{scale} and $P_{threshold}$ for the given dataset have been set as 0.8 and $10,000$, respectively.

The segmentation masks corresponding to each method are represented by the green outlines in their respective segmentation figures in Figs. 5, 6, 7, and 8. The blue outlines denote segmentations that are problematic, covering cases of false positives, over-segmentations, and under-segmentations.

The graph shown in Fig. 5 illustrates the point at which M_{SD} begins to consider densely populated cells as a single unit, whereas M_{CP} ignores these regions entirely. The utilization of M_{SD} is intended to improve cell counts in densely populated regions as the primary goal of this study.

Both Fig. 5 and Fig. 6 show false-positive cell detection in low-intensity areas due to background interference. However, the impact of these extra cells is negligible since they can be readily eliminated through thresholding or similar methodologies.

The segmentation outcomes of all methodologies for the D_{C4} dataset are shown in Fig. 7 and Fig. 8. Despite a few variations in the count results, the segmentation results show a high degree of similarities. It is challenging to make comparisons or observe enhancements as both M_{CP} and M_{SD} show near-perfect performance for images that are relatively simple to process. Table 2 displays the error percentages for each dataset. Although the benchmark datasets yield very similar results, M_E can deliver the advantages of both models when dealing with more complex datasets.

Dataset	(M_E)	M_{CP}	M_{SD}
D_{C4}	10.17%	10.06%	13.28%
D_{C39}	11.64%	11.74%	12.04%
D_{ORIG}	78.19%	87.30%	271.37%

TABLE 2. **Cell count error percentages for each dataset and method.**

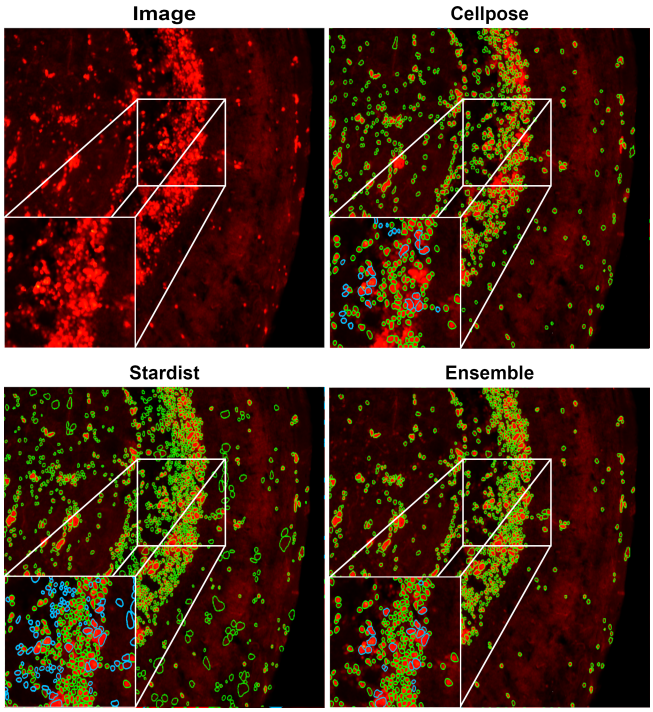

FIGURE 5. **A portion of the segmentation results for an image from D_{ORIG} where both methodologies under-segment.**

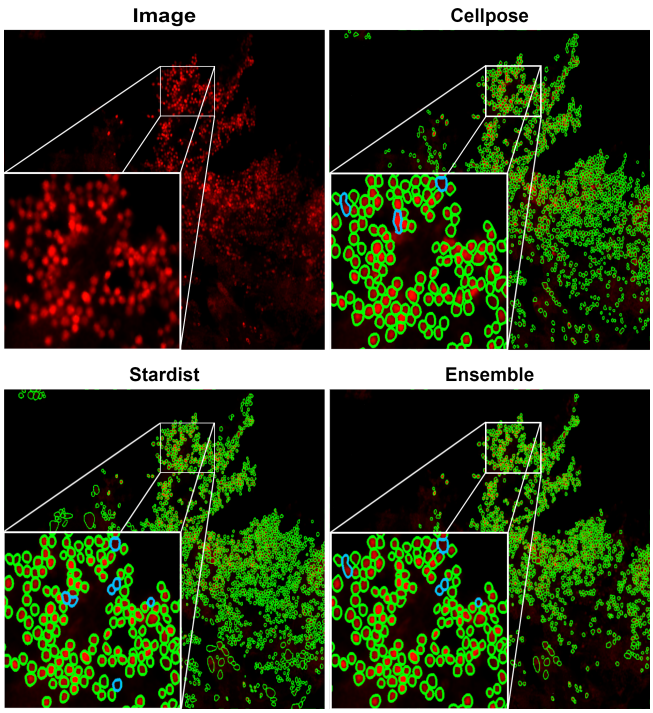

FIGURE 6. **A portion of the segmentation results for an image from D_{ORIG} where both methodologies over-segment.**

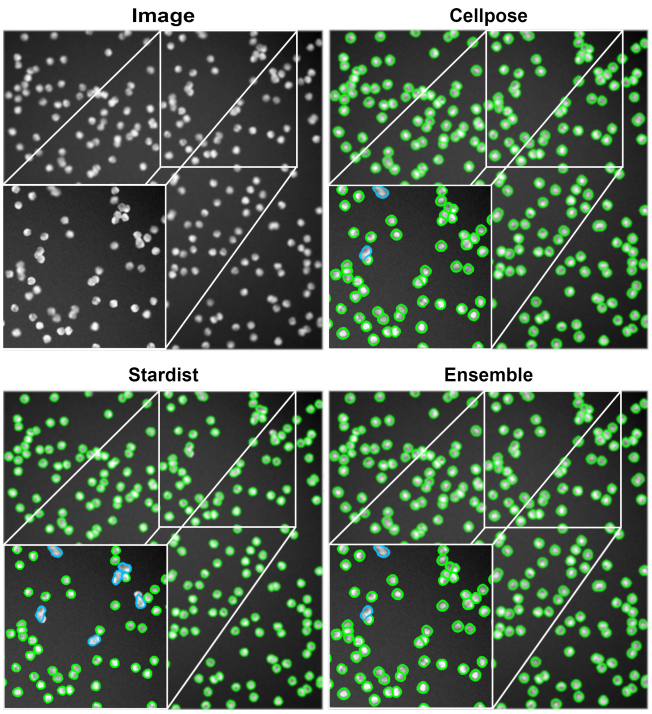

FIGURE 7. A portion of the segmentation results for an image with 15% overlap probability in D_{C4}.

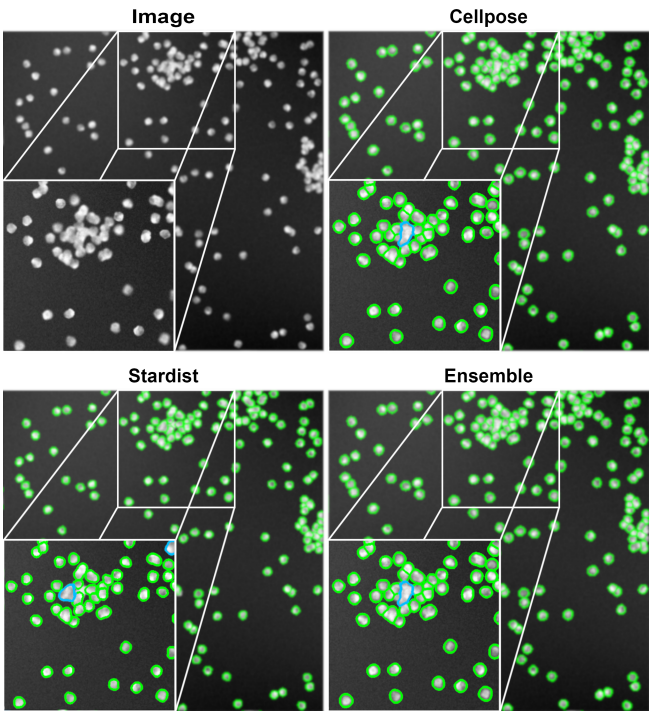

FIGURE 8. A portion of the segmentation results for an image with 60% overlap probability in D_{C4}.

C. PARAMETER ANALYSIS

Despite the observations of enhancements across all datasets, the proposed approach showed constraints for specific images. In the context of our experimentation, it was observed that there were cases where the accuracy of the results obtained from M_E was comparatively lower than those obtained from M_{CP} and M_{SD}. This section will discuss the external parameters that we used and their effects on the ensemble process.

As stated previously, the scaling factor P_{scale} is used to reduce the value of Otsu's threshold. This phenomenon improves the ability of M_E to detect cell clusters showing lower brightness levels, thereby increasing the recall rate of the algorithm. As a result, the proposed approach is expected to improve the detection of a more significant number of cells that also exist in the ground truth. Nonetheless, a lower scale may increase the algorithm's potential for tissue noise. Regions with high background brightness (and a lower contrast difference in the cells) are more responsible for generating false positives. Fig. 10 shows the error percentage for different P_{scale} values when the $P_{threshold}$ is set to $10,000$. The error percentage is mostly stable for the P_{scale} values under 1. As P_{scale} goes above 1, the error percentage starts to increase due to information loss.

The usage rates of S_{CP} and S_{SD} are determined by the value of $P_{threshold}$. Selecting a threshold value that is either excessively high or excessively low may result in the nullification of the proposed approach's effects, as the algorithm will show a preference for one segmentation result over the other. If the value is set too high, the count results will converge to the M_{CP} results, whereas if it is set too low, the count results will converge to the M_{SD} results. When selecting a suitable $P_{threshold}$, cell size (in terms of pixels) should be considered. Since this parameter helps separate regions of different sizes, Eq. 1 can help determine an approximate area threshold for regions. Fig 9 shows the error percentage for different $P_{threshold}$ values. The variation of the error is mostly under 1% when the P_{scale} is 0.8. The stability of the error percentage in Fig. 10 and Fig. 9 indicates robustness to variations in our external parameters. While these parameters influence the result, they don't have to be exact to produce near-optimal results.

$$P_{\text{threshold}} = \text{NOC} \times \pi \times \text{ACR}^2 \tag{1}$$

where NOC and ACR denote the number of cells and average cell radius, respectively.

V. CONCLUSION

Cellpose and Stardist are acknowledged as two of the most sophisticated image segmentation models currently available, providing robust solutions for a diverse array of research applications. Despite their advanced capabilities, these models face substantial challenges when processing images with densely populated cell clusters and interference from surrounding tissue. Such complexities frequently result in segmentation inaccuracies that are not easily remedied through

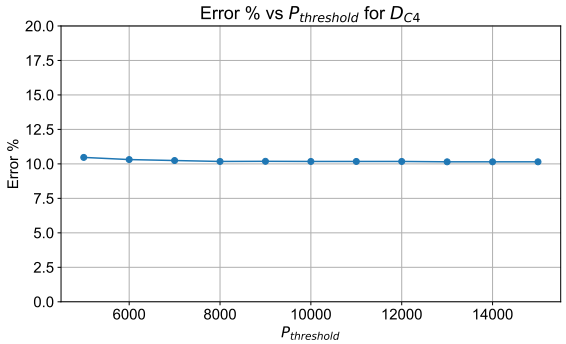

FIGURE 9. **Average error % for different $P_{threshold}$ with P_{scale} set to 0.8 for D_{C4}. The X-axis denotes different $P_{threshold}$ values and Y-axis denotes the average error % of the dataset.**

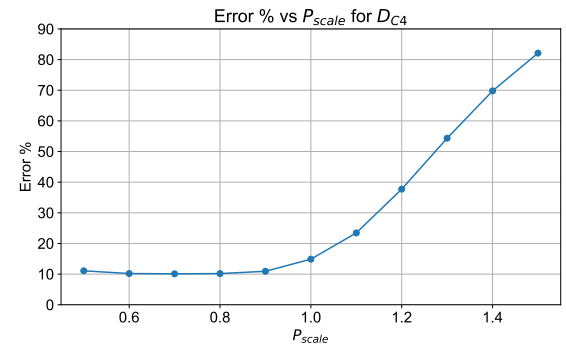

FIGURE 10. **Average error % for different P_{scale} values with $P_{threshold}$ set to 10,000 for D_{C4}. The X-axis denotes different P_{scale} values, and the Y-axis denotes the average error % of the dataset.**

additional training. The primary impediment to further training is the prohibitive cost associated with the extensive annotation procedures required to enhance model performance.

This study introduces an innovative approach by demonstrating the efficacy of ensembling state-of-the-art models to address these segmentation challenges. By integrating the strengths of multiple models, the ensemble method significantly reduces errors in cell counting assignments, particularly in scenarios where further training is not feasible. This novel technique not only enhances accuracy but also offers a cost-effective alternative to traditional model retraining.

Our study relies on the integration of two state-of-the-art segmentation models to enhance segmentation performance without necessitating additional training. Consequently, the efficacy of our approach is significantly contingent upon these models. Prospective studies will explore the potential for incorporating additional models via ensembling to refine the accuracy of the results.

Another future direction could focus on optimizing ensemble strategies to further improve segmentation outcomes. Additionally, the development of adaptive algorithms that can dynamically adjust to varying image complexities holds promise for advancing the field. Exploring the integration of other state-of-the-art machine learning techniques that require minimal annotation could also provide valuable insights, paving the way for more efficient and scalable solutions in cell segmentation and detection.

REFERENCES

[1] N. F. Greenwald *et al.*, "Whole-cell segmentation of tissue images with human-level performance using large-scale data annotation and deep learning," *Nature Biotechnology*, vol. 40, pp. 555–565, 2021.
[2] J. C. Caicedo *et al.*, "Nucleus segmentation across imaging experiments: the 2018 data science bowl," *Nature Methods 16:12*, pp. 1247–1253, 2019.
[3] G. Giacopelli, M. Migliore, and D. Tegolo, "Neuronalg: An innovative neuronal computational model for immunofluorescence image segmentation," *Sensors*, vol. 23, p. 4598, 2023.
[4] C. Stringer, T. Wang, M. Michaelos, and M. Pachitariu, "Cellpose: a generalist algorithm for cellular segmentation," *Nature Methods*, vol. 18, 2021.
[5] M. Pachitariu and C. Stringer, "Cellpose 2.0: how to train your own model," *Nature Methods*, vol. 19, pp. 1634–1641, 2022.
[6] U. Schmidt, M. Weigert, C. Broaddus, and G. Myers, "Cell detection with star-convex polygons," pp. 265–273, Springer Verlag, 2018.
[7] C. F. Koyuncu, S. Arslan, I. Durmaz, R. Cetin-Atalay, and C. Gunduz-Demir, "Smart markers for watershed-based cell segmentation," *PLOS ONE*, vol. 7, p. e48664, 2012.
[8] C. F. Koyuncu, E. Akhan, T. Ersahin, R. Cetin-Atalay, and C. Gunduz-Demir, "Iterative h-minima-based marker-controlled watershed for cell nucleus segmentation," *Cytometry Part A*, vol. 89, pp. 338–349, 2016.
[9] C. F. Koyuncu, R. Cetin-Atalay, and C. Gunduz-Demir, "Object-oriented segmentation of cell nuclei in fluorescence microscopy images," *Cytometry Part A*, vol. 93, pp. 1019–1028, 2018.
[10] M. Hayat and S. Aramvith, "E-sevsr—edge guided stereo endoscopic video super-resolution," *IEEE Access*, vol. 12, pp. 30893–30906, 2024.
[11] M. Hayat and S. Aramvith, "Saliency-aware deep learning approach for enhanced endoscopic image super-resolution," *IEEE Access*, vol. 12, pp. 83452–83465, 2024.
[12] L. Lupori *et al.*, "A comprehensive atlas of perineuronal net distribution and colocalization with parvalbumin in the adult mouse brain," *Cell Reports*, vol. 42, p. 112788, 2023.
[13] C. F. Koyuncu, G. N. Gunesli, R. Cetin-Atalay, and C. Gunduz-Demir, "Deepdistance: A multi-task deep regression model for cell detection in inverted microscopy images," *Medical Image Analysis*, vol. 63, p. 101720, 2020.
[14] L. Ciampi *et al.*, "Learning to count biological structures with raters' uncertainty," *Medical Image Analysis*, vol. 80, p. 102500, 2022.
[15] A. Arslan-Ergul *et al.*, "Short-term dietary restriction in old zebrafish changes cell senescence mechanisms," *Neuroscience*, vol. 334, pp. 64–75, 2016.
[16] C. A. Beretta *et al.*, "Quanty-cfos, a novel imagej/fiji algorithm for automated counting of immunoreactive cells in tissue sections," *Cells*, vol. 12, p. 704, 2023.
[17] A. Sekar *et al.*, "Rapid cell counter: Semi-automated and mid-throughput estimation of cell density within diverse cortical layers," *Eneuro*, vol. 8, 2021.
[18] D. Cadena-Herrera *et al.*, "Validation of three viable-cell counting methods: Manual, semi-automated, and automated," *Biotechnology Reports*, vol. 7, pp. 9–16, 2015.
[19] Y. Zhao, X. Wang, T. Che, G. Bao, and S. Li, "Multi-task deep learning for medical image computing and analysis: A review," *Computers in Biology and Medicine*, vol. 153, p. 106496, 2023.
[20] J. Xu *et al.*, "Deep learning in cell image analysis," *Intelligent Computing*, vol. 2022, 2022.
[21] G. Kleinberg, S. Wang, E. Comellas, J. R. Monaghan, and S. J. Shefelbine, "Usability of deep learning pipelines for 3D nuclei identification with stardist and cellpose," *Cells & Development*, vol. 172, p. 203806, 2022.
[22] O. Sagi and L. Rokach, "Ensemble learning: A survey," *Wiley Interdisciplinary Reviews: Data Mining and Knowledge Discovery*, vol. 8, p. e1249, 2018.
[23] M. Kuko and M. Pourhomayoun, "An ensemble machine learning method for single and clustered cervical cell classification," in *Proc. IEEE International Conference on Information Reuse and Integration for Data Science (IRI)*, pp. 216–222, 2019.
[24] C. H. C. Pena, T. I. Ren, P. D. M. Fernandez, F. A. Guerrero-Peña, and A. Cunha, "An ensemble learning method for segmentation fusion," in

Proc. International Joint Conference on Neural Networks (IJCNN), pp. 1–6, 2022.

[25] P. Tang, X. Yang, Y. Nan, S. Xiang, and Q. Liang, "Feature pyramid nonlocal network with transform modal ensemble learning for breast tumor segmentation in ultrasound images," *IEEE Transactions on Ultrasonics, Ferroelectrics, and Frequency Control*, vol. 68, pp. 3549–3559, 2021.

[26] L. Wu, A. Chen, P. Salama, K. W. Dunn, and E. J. Delp, "An ensemble learning and slice fusion strategy for three-dimensional nuclei instance segmentation," in *Proc. IEEE/CVF Conference on Computer Vision and Pattern Recognition Workshops (CVPRW)*, pp. 1883–1893, 2022.

[27] M. G. Haberl *et al.*, "Cdeep3m—plug-and-play cloud-based deep learning for image segmentation," *Nature Methods*, vol. 15, pp. 677–680, 2018.

[28] C. Shen *et al.*, "Automatic detection of circulating tumor cells and cancer associated fibroblasts using deep learning," *Scientific Reports*, vol. 13, pp. 1–13, 2023.

[29] A. Goodman *et al.*, "2018 data science bowl," 2018.

[30] O. Ronneberger, P. Fischer, and T. Brox, "U-net: Convolutional networks for biomedical image segmentation," in *Proc. International Conference on Medical Image Computing and Computer-Assisted Intervention (MICCAI)* (N. Navab, J. Hornegger, W. M. Wells, and A. F. Frangi, eds.), (Cham), pp. 234–241, Springer International Publishing, 2015.

[31] A. Lehmussola, P. Ruusuvuori, J. Selinummi, H. Huttunen, and O. Yli-Harja, "Computational framework for simulating fluorescence microscope images with cell populations," *IEEE Transactions on Medical Imaging*, vol. 26, pp. 1010–1016, 2007.

[32] A. Lehmussola, P. Ruusuvuori, J. Selinummi, T. Rajala, and O. Yli-Harja, "Synthetic images of high-throughput microscopy for validation of image analysis methods," *Proceedings of the IEEE*, vol. 96, pp. 1348–1360, 2008.

[33] V. Ljosa, K. L. Sokolnicki, and A. E. Carpenter, "Annotated high-throughput microscopy image sets for validation," *Nature Methods 2012*, vol. 9, pp. 637–637, 2012.

C. EMRE DEDEAGAC received his B.Sc. degree from the Department of Electrical and Electronics Engineering at Ozyegin University in 2020 with a minor in Computer Science. He has worked on various research projects throughout his academic life; subjects include but are not limited to machine learning, computer arithmetic, and high frequency trading. He is now doing a direct Ph.D. in Computer Science at Ozyegin University, and his current research topics include ASIC/SoC/FPGA design/automation, neural network accelerators, and computer arithmetic.

CAN F. KOYUNCU is a machine learning (ML) and computer vision scientist with an extensive background in applying and developing AI on real-life problems. Prior to Meta, he was a Research Assistant Professor in the Wallace H. Coulter Department of Biomedical Engineering at Emory University and Georgia Tech. During this time, Dr. Koyuncu has been awarded a $644k grant for his novel prognostic and diagnostic ML/computer vision approaches under the category of the Career Development Award funded by the Department of Defense (DoD). He has a full stack of skills covering the whole life-cycle of ML/deep learning approaches, including exploratory data analysis, feature engineering, model building, evaluation, and monitoring.

MICHELLE M. ADAMS received her Ph.D. in Neuroscience in 2001 from the New York University - Mount Sinai School of Medicine. Her Ph.D. work focused on the relationship among brain aging, cognitive decline, estrogen, and glutamate receptors. Dr. Adams did a postdoctoral fellowship at the HHMI in Brown/MIT examining the functional consequences of altering glutamate receptor levels and then in 2004, she went to the Neurobiology and Anatomy Department at Wake Forest University School of Medicine to study the effects of caloric restriction on synaptic glutamate receptors. In 2005, Dr. Adams became an assistant professor at Wake Forest University, and then in 2009 she moved to Bilkent University where she is currently a professor and chair of the Psychology Department. Her work has been published in a number of journals, including Nature, PNAS, Journal of Neuroscience and Neurobiology of Aging.

CAGATAY EDEMEN received B.Sc. degree from Marmara University and the Ph.D. degree from Işık University in Electronics Engineering. He is currently an assistant professor at Ozyegin University. Dr. Edemen has been working on several research projects with a focus on information theory, communication theory, and networks in wireless systems. In particular, he conducts research on information theoretic aspects of multi-user cooperative communication. Another field of recent interest for him is the field of optical communication. In particular, he is interested in the applications of Visible Light Communication. He holds both national and international patents in this area. Dr. Edemen was awarded the IEEE WCNC Best Paper Award and IEEE SIU Communication Society Best Paper Award for his works titled "Achievable Rates for the Three User Cooperative Multiple Access Channel" and "Channel Modeling of Reconfigurable Intelligent Surfaces-aided Underwater Acoustic Communication System".

BERK C. UGURDAG is an undergraduate student pursuing a Bachelor of Science in computer science at Georgetown University in Washington, DC. He graduated from Robert College in Istanbul in 2022 and expects to graduate from Georgetown University in 2026. His interests are artificial intelligence, computational biology, and data science.

N. ILGIM ARDIC-AVCI received her bachelor's degree from the Department of Psychology and master's degree from the Department of Neuroscience in Bilkent University. During her master's study, she studied age-related neuronal and glial changes in zebrafish. She is currently a PhD candidate in the Department of Neuroscience under the supervision of Prof. Michelle Adams of Bilkent University. Her current research focuses on the environmental and genetic contributions to inflammation and its associated oxidative stress during brain aging using zebrafish as a model organism.

H. FATIH UGURDAG received the BS degree from Bogazici University, Istanbul, Turkey, in 1986, with a double major in EE and Physics, and the MS and PhD degrees in EE from Case Western Reserve University, Cleveland, Ohio in 1989 and 1995, respectively. He is currently a Full Professor at Ozyegin University, Istanbul, Turkiye. He is also a long-time IEEE volunteer. He was recently the Chair of the IEEE Turkiye Section. He worked full-time in the industry for 13 years before joining academia, in 2004. His tenure in the industry was mostly in Silicon Valley and involved companies such as GE, GM, Lucent, Juniper, Nvidia. His research interests include ASIC/SoC/FPGA implementation of various compute-intensive algorithms, design automation, and computer arithmetic.